arXiv:1402.4134v2 [astro-ph.HE] 6 Jul 2014

Two-Dimensional Simulations of Pulsational Pair-Instability Supernovae

Ke-Jung Chen[1,2,*], Stan Woosley[1], Alexander Heger[3], Ann Almgren[4] and Daniel J. Whalen[5,6]

Received _____; accepted _____

[*]IAU Gruber Fellow; kchen@ucolick.org

[1]Department of Astronomy & Astrophysics, University of California, Santa Cruz, CA 95064, USA

[2]School of Physics and Astronomy, University of Minnesota, Minneapolis, MN 55455, USA

[3]Monash Centre for Astrophysics, Monash University, Victoria 3800, Australia

[4]Center for Computational Sciences and Engineering, Lawrence Berkeley National Lab, Berkeley, CA 94720, USA

[5]T-2, Los Alamos National Laboratory, Los Alamos, NM 87545, USA

[6]Zentrum für Astronomie, Institut für Theoretische Astrophysik, Universität Heidelberg, Albert-Ueberle-Str. 2, 69120 Heidelberg, Germany

ABSTRACT

Massive stars that end their lives with helium cores in the range of 35 to 65 $M_\odot$ are known to produce repeated thermonuclear outbursts due to a recurring pair-instability. In some of these events, solar masses of material are ejected in repeated outbursts of several times 10^{50} erg each. Collisions between these shells can sometimes produce very luminous transients that are visible from the edge of the observable universe. Previous 1D studies of these events produce thin, high-density shells as one ejection plows into another. Here, in the first multi-dimensional simulations of these collisions, we show that the development of a Rayleigh-Taylor instability truncates the growth of the high density spike and drives mixing between the shells. The progenitor is a 110 $M_\odot$ solar-metallicity star that was shown in earlier work to produce a superluminous supernova. The light curve of this more realistic model has a peak luminosity and duration that are similar to those of 1D models but a structure that is smoother.

Subject headings: stars: early-type – supernovae: general – stars: supernovae – nuclear reactions – radiative transfer – hydrodynamics – cosmology:theory – stars: Population II – instabilities

1. Introduction

The idea of a "pulsational pair-instability supernova" (PPISN) was introduced by Barkat et al. (1967) and explored in some detail by Woosley et al. (2007). For a range of helium core masses above approximately 35 $M_{\odot}$, the production of electron-positron pairs occurs during central neon burning and triggers an instability that leads to rapid contraction of the core and explosive nuclear burning. If the helium core mass is above about 65 $M_{\odot}$, the pair production instability occurs after carbon ignition and the energy released can completely unbind the star in a single explosive event known as a pair-instability supernova (PISN; Heger & Woosley 2002; Scannapieco et al. 2005; Chatzopoulos & Wheeler 2012a; Chatzopoulos et al. 2013; Chen et al. 2014). If the core mass is above 133 $M_{\odot}$, for reasonable nuclear reaction rates, convection theory, and no rotation, nuclear burning is unable to reverse the collapse and a black hole forms (Heger & Woosley 2002).

For helium core masses from 35 - 65 $M_{\odot}$, Although explosive burning is violent and energetic, it cannot unbind the entire star, and cycles of instability and mass ejection can instead occur. The energy, duration, and mass ejected by these nuclear-powered pulses increases as the helium core mass rises, and by about 45 $M_{\odot}$ they are sufficient to produce SN-like displays (Woosley et al. 2007; Vink 2014). If the helium core is capped by a substantial hydrogen envelope, the first strong pulse ejects it. Depending on the radius and mass of the envelope, this initial ejection may give rise to either a faint or rather typical Type IIp SN. Subsequent pulses later overtake and collide with the first and produce a much brighter Type IIn SN. If there is no hydrogen envelope, collisions between helium shells can produce a bright Type I SN. The helium core mass range from 45 to 55 $M_{\odot}$ is particularly interesting because the characteristic time scale between pulsations is years and the collisions between shells ejected with speeds $\sim$ 1000 km s^{-1} occur at 10^{15} - 10^{16} cm, where the collision energy is mostly dissipated by optical emission. Since the collision

energy can approach 10^{51} erg, a superluminous event can result.

The discovery of both PI and PPI SN candidates in the local universe, and the realization that such events might be visible at high redshifts, have excited interest in this exotic explosion mechanism. SN 2007bi at $z = 0.127$ (Gal-Yam et al. 2009) and SN 2213-1745 at $z = 2.06$ (Cooke et al. 2012) are PISN candidates, and SN 1000+0216 at $z = 3.90$ (Cooke et al. 2012) and perhaps SN 2006oz at $z = 0.376$ (Leloudas et al. 2012) may be PPISNe. Dessart et al. (2013) suggest that SN 2007bi may be a magnetar spin-down powered event (Kasen & Bildsten 2010; Woosley 2010; Dessart et al. 2012) or it could be due to an interaction between H-poor SN ejecta and a circumstellar medium (Chatzopoulos & Wheeler 2012b; Moriya et al. 2013). The nature of these transients is still under debate. Whalen et al. (2014) have now shown that PPISNe, like PISNe and Type IIne, may be visible to the *James Webb Space Telescope* (*JWST*) and the Wide-Field Infrared Survey Telescope (WFIRST) at $z \sim 20$ (see also Kasen et al. 2011; Pan et al. 2012; Whalen et al. 2013c,a,d; Hummel et al. 2012). These explosions, together with other Population III (Pop III) SNe (Joggerst et al. 2010; Whalen et al. 2013b,e; Johnson et al. 2013), could probe the properties of the first stars and galaxies (Bromm et al. 2009; Glover 2013; Whalen 2012; Bromm & Yoshida 2011), early cosmological reionization and chemical enrichment (Whalen et al. 2004; Mackey et al. 2003; Smith & Sigurdsson 2007; Smith et al. 2009; Ritter et al. 2012; Safranek-Shrader et al. 2013), and the origins of supermassive black holes (Volonteri 2012).

Understanding the observational signatures of PPISNe is key to properly identifying them as more of them are discovered by the new SN factories such as the Palomar Transient Factory (PTF; Law et al. 2009), the Panoramic Survey Telescope and Rapid Response System (Pan-STARRS; Kaiser et al. 2002) and the Large Synoptic Survey Telescope (LSST; Ivezic et al. 2008). High-z SN surveys by *JWST* and WFIRST may harvest even

greater numbers of PPISNe if, as many suspect, the Pop III initial mass function (IMF) is top-heavy. Woosley et al. (2007) modeled a PPISN in one dimension (1D) with the KEPLER code (Weaver et al. 1978; Heger et al. 2001) and its light curve with the STELLA code (Blinnikov et al. 2006). In these simulations, a large density spike formed during the collision between the second two pulses and the first. Rapid variations in the density of the spike due to a radiative instability (Chevalier & Imamura 1982; Imamura et al. 1984) imposed large fluctuations in the bolometric luminosity. Whalen et al. (2014) noted similar features in the near infrared (NIR) light curves of the same PPISN modeled with the Los Alamos RAGE code. Such spikes would probably not appear in multidimensional flows because hydrodynamic instabilities would likely erase the sharp interface between the pulses. It is not clear how these processes would change the luminosity of the collision.

Radiation hydrodynamical simulations in at least two dimensions (2D) with adaptive mesh refinement (AMR) are clearly required to resolve the thin radiating region between the shells during the collision and properly model the light curves of PPISNe. But such simulations push the envelope of even state-of-the-art numerical codes. As a first step to this goal, we have performed the first 2D simulations of a PPISN with the CASTRO code with hydrodynamics but not radiation transport. In Section 2 we describe our PPISN model and how it is evolved in CASTRO. In Section 3 we examine the collision of the shells in 2D in detail, and in Section 4 we show how the evolution of the collision in 2D might change the PPISN light curves of previous calculations. We conclude in Section 5.

2. PPISN Model / Numerical Method

We take as a fiducial case the PPISN examined in Woosley et al. (2007), whose progenitor was a solar-metallicity star with an initial main sequence mass of 110 $M_\odot$. The mass loss rate was artificially reduced so that the star had a total mass of 74.6 $M_\odot$ and

a helium core mass of 49.9 $M_\odot$ when it died. The star produces three violent outbursts. The first, P1, ejects most of the hydrogen envelope, making a faint Type II supernova and leaving a residual of 50.7 $M_\odot$, just a bit more than the helium core itself. After 6.8 yr, the core again contracts and encounters the pair instability, twice in rapid succession. The total mass of the second and third pulses (P2 and P3) is 5.1 $M_\odot$ and their kinetic energy is 6×10^{50} erg. P3 collides with P2 at large optical depths that are not visible to an external observer. These combined shells then overtake P1 at $\sim 10^{15}$ cm and speeds of a few 1000 km s^{-1}. About 90% of the energy of this collision is radiated away by 10^{16} cm, with peak bolometric luminosities of $\sim 3 \times 10^{43}$ erg sec^{-1}.

2.1. CASTRO

CASTRO is a multi-dimensional AMR astrophysical fluid dynamics code (Almgren et al. 2010; Zhang et al. 2011). It has an unsplit piecewise parabolic method (PPM) hydro scheme (Colella & Woodward 1984) and multispecies advection. The equation of state used in our study was taken from Timmes & Swesty (2000), and has contributions from relativistic e^-e^+ pairs of arbitrary degeneracy, ions, which are treated as an ideal gas, and photons. Densities, velocities, temperatures and mass fractions from KEPLER were mapped onto a 2D cylindrical grid in CASTRO with the conservative scheme of Chen et al. (2011); Chen et al. (2013), which guarantees that quantities such as energy and mass are strictly conserved. Because only one quadrant of the star is mapped onto the mesh, outflow and reflecting boundary conditions were set on the upper and lower boundaries in r and z, respectively. Three levels of adaptive refinement (for up to 64 times greater resolution along each axis) were used to resolve the scales on which instabilities form in the flow, and the grid refinement criteria are based on gradients of density, velocity, and pressure. We use the monopole approximation for self-gravity, in which a 1D gravitational potential

is constructed from the radial average of the density and then applied to gravitational force updates everywhere in the AMR hierarchy. This approximation is very efficient, and well-suited to the nearly spherical symmetry of the star and its pulsations.

3. PPISN Evolution

3.1. Fallback

In principle, partial fallback from one pulse could collide with a subsequent ejection and seed the formation of instabilities and mixing before the pulses themselves collide. We investigate this process with a 2D simulation in `CASTRO` in which we follow fallback from P2 onto P3. This simulation must be performed on a much smaller mesh that excludes P1 in order to resolve the length scales of nuclear burning, which powers the pulses, and the onset of any fluid instabilities near the core. It is initialized with a `KEPLER` output at an intermediate time from Woosley et al. (2007), $\sim$ 100 sec before P2. Our `CASTRO` mesh is 5 $\times$ 10^{13} cm on a side with 256^2 zones at the coarsest level. As in `KEPLER`, nuclear burning is calculated with a 19-isotope network that includes species from hydrogen through ^{56}Ni (Weaver et al. 1978). The star is evolved until the expulsion of P3.

Gas velocities and densities at the end of this run are shown in Figure 1. Fallback from P2 does trigger mild perturbations in the velocities near the surface of P3, on the order of a few percent of the local sound speed, but they do not result in any discernible features in the densities. This simulation demonstrates that launching collision models in `CASTRO` from `KEPLER` snapshots at later times will not exclude serious dynamical instabilities originating from fallback at earlier times. Modeling perturbations in the gas due to fallback from all three pulses at the same time at the required resolution would require a grid that is four orders of magnitude larger than this one, so we approximate these features in our collision

models by seeding the grid with random velocity perturbations of order about 1 % of local sound speed.

3.2. First Collision

To study the collisions between the three pulses, we initialize CASTRO with a KEPLER profile taken at a later time, after all three eruptions have occurred and when P1 is at 2 × 10^{16} cm, as shown in Figure 2. Since Woosley et al. (2007) and Whalen et al. (2014) both predict that most of the radiation from the collision between shells P2/P3 and P1 is emitted by the time the shock has reached 10^{16} cm, we set the outer boundaries of the grid in r and z to be 10^{16} cm. We do not include all of P1 in our simulation because the density beyond 10^{16} cm is extremely low and most fluid instabilities forming during collisions have become frozen in mass coordinate before reaching this boundary. With AMR, the effective spatial resolution can be as fine as 10^{12} cm, which is sufficient for capturing the fine structure of each pulse, as we show in Figure 3) and fluid instabilities in the flow later on. All three pulses are evolved until the collision shock reaches the simulation boundary, about 260 days after the launch of the run.

At the beginning of the simulation, the peak velocities of P2 and P3 are 3.9 × 10^7 cm s^{-1} and 4.8 × 10^7 cm s^{-1}, respectively. The faster P3 overtakes P2 within 50 days and has completely merged with it at $r \sim 2.3 \times 10^{15}$ cm. The contact discontinuity that forms between P3 and P2 upon collision rapidly destabilizes into the mild, finger-like fluid instabilities that are visible at 2.5 × 10^{15} cm in Figure 4. These fingers are 2 - 3×10^{14} cm in size, with overdensities of 5 - 10. The combined pulse has a complex structure with multiple velocity peaks, the highest of which is 4.7 × 10^7 cm s^{-1}. The bright emission from this collision is probably not visible to an external observer because it originates from very optically thick regions that are well below the photosphere at ∼ 8 ×10^{15} cm. Nevertheless,

this radiation may be able affect the dynamics of the ejecta or diffuse out of it at later times.

3.3. The Second Collision

After P2 and P3 collide, they together begin to overtake P1, which now has a radius 100 times that of the original star. Unlike the first collision, the second collision is more like that between supernova ejecta and a dense shell expelled by the star prior to its death (Type IIn SNe, e.g., Whalen et al. 2013d; Moriya et al. 2013). Although this collision is less violent than a Type IIn SN, the instabilities eventually grow to larger amplitudes than in the first collision, as we show in Figure 5. The clumpy structures behind the shock grow in size as the flow expands, driving more mixing and dredging up heavier elements from deeper layers. We plot angle-averaged mass fractions for ^{4}He, ^{12}C, ^{16}O, and ^{24}Mg in Figure 6 as the shock approaches the photosphere. Most mixing happens by $\sim 10^{16}$ cm, and elements heavier than ^{28}Si remain deeper in the ejecta, so they would not appear in the spectra.

The formation of dynamical instabilities during the collisions can be understood on analytical grounds. Both times, the instabilities appear because the shock decelerates as it plows up gas and forms a reverse shock. For a strong adiabatic shock in a power-law density profile, $\rho = Ar^{w}$, the flow becomes self-similar, and the physical quantities that describe it can be combined into a single, dimensionless function, $f_w(A, E, t)$, where E is the explosion energy and t is the time (Sedov 1959; Herant & Woosley 1994). The velocity of the shock can then be derived from dimensional analysis:

$$V_{\rm s} = A^{\frac{-1}{(5+w)}} E^{\frac{1}{(w+5)}} t^{\frac{-(w+3)}{5+w}}. \quad (1)$$

For $w > -3$, the shock decelerates as it plows up material. This deceleration is communicated to the fluid behind by the shock at the sound speed, and it creates a pressure

gradient in the direction of the deceleration. The sound wave generated by the deceleration can steepen this pressure gradient, and a reverse shock forms. If the gas pressure, P, and the density, ρ, satisfy the Rayleigh-Taylor (RT) criterion for an fluid (Chandrasekhar 1961)

$$\frac{\mathrm{d}P}{\mathrm{d}r}\frac{\mathrm{d}\rho}{\mathrm{d}r} < 0, \tag{2}$$

then instabilities will form. Whether or not a reverse shock forms can be determined by the ρr^3 profile in the surrounding medium. If ρr^3 increases with radius, conditions are favorable for the formation of a reverse shock. We plot this quantity for the time at which our `CASTRO` run is launched in Figure 8. The peaks and valleys at $r < 10^{15}\,\mathrm{cm}$ were created by the ejection of P2 and P3. The acceleration and deceleration of the shock in this rapidly varying region causes the smaller fluid instabilities in the first collision shown in Figure 4. The steady increase in ρr^3 at $r \geq 10^{15}\,\mathrm{cm}$ leading up to P1 allows the instabilities to grow to larger amplitudes during the second collision. When the RT fingers become nonlinear, Kelvin-Helmholtz (or shear) instabilities arise and dominate the mixing, which continues until the collision shock breaks through P1. Figure 7 shows the AMR grid structure when the mixing occurs. Many fine grids are generated to resolve the clumpy structure due to mixing.

3.4. Light Curve

Most of the luminosity from the second collision is gone before mixing ends. We approximate the bolometric light curve of this collision by (Chevalier & Irwin 2011, 2012):

$$L_* = 2\pi\rho r^2 v_s^3, \tag{3}$$

where ρ is the gas density just ahead of shock front, v_s is the velocity of the shock, and r is the position of the shock. Equation (3) holds if the region in which the shock propagates is assumed to be optically thin, and is therefore an upper limit in somewhat higher densities.

To take into account energy dissipation in the shock by escaping photons, we assume that the luminosity of the shock falls as r^{-2} when the shock front is beyond $\sim 5 \times 10^{15}$ cm. We assume that the temperature at the edge of the shock falls as $T \propto r^{-1}$ due to thermal radiation, so the bolometric luminosity $L_* \propto r^2 T^4 \propto r^{-2}$. We plot this luminosity in Figure 9. The collision produces a very bright transient, with a peak luminosity of $\sim 4 \times 10^{43}$ erg sec^{-1} and a duration of ~ 100 days. The peak luminosity occurs when P2+P3 collide with P1. Its magnitude is calculated with Equation (3), with $\rho = 1.03 \times 10^{-14}$ g cm^{-3}, $r = 2.46 \times 10^{15}$ cm, and $v_s = 4.52 \times 10^8$ cm/s. The peak luminosity and duration are similar to those of the 1D radiation hydrodynamics models of Woosley et al. (2007) and Whalen et al. (2014). But our light curve rises earlier because we assume that the environment of the shock is optically thin. Unlike the 1D light curves, which exhibit artificial fluctuations due to a radiative instability, the light curve of our 2D model has a relatively smooth peak and no fluctuations. Our model suggests that radiation hydrodynamical calculations of PPISN light curves in 2D will also be smoother than those in 1D because mixing will dampen the radiative instability, but that they will have similar luminosities. We calculate 2D light curves with Equation (3) with angle-averaged densities and velocities at radii just ahead of the shock. This light curve is a rough estimate of the luminosity of the shock and does not include radiation from dense clumps due to shell collisions. Although the 2D light curve has similar luminosities to 1D models, the light curve rising time and fading tail are still quite different between 1D and 2D. Full radiation transport in 2D is needed for more realistic light curves of PPISN models.

4. Conclusion

We have performed the first 2D hydrodynamical simulations of PPISNe with the new `CASTRO` code. We find that mild RT instabilities develop first during the collision of P3 with

P2 and then become stronger as P2 and P3 interact with P1. Fallback from one pulsation onto another does not seed strong instabilities but does mildly perturb the flow prior to collisions. The appearance of dynamical instabilities and mixing has three consequences for the observational signatures of PPISNe that are not captured in 1D models.

First, the radiative instabilities that cause light curves to fluctuate in 1D models probably do not happen in actual explosions. Mixing between shells dampens the formation of the density spikes in 1D models that give rise to these features. Second, the formation of dense clumps by RT fingers could trap photons and alter the luminosity of these events. We neglect radiative cooling by metals and dust in our models so these clumps may catastrophically cool and become much denser (and more opaque) in actual collisions. This in turn could amplify the RT instabilities. Finally, since mixing is strongest in the region of the flow from which most of the luminosity of the collision originates, it will alter the order in which specific absorption and emission lines appear in the spectrum over time. In particular, our model predicts enhanced spectral lines from ^{12}C and ^{16}O at earlier times in the second collision. The appearance of such lines may prove to be powerful diagnostics of mixing in PPISNe.

Since our approximate bolometric luminosities are similar to those calculated with full radiation transport in earlier work, future multidimensional calculations will probably not change the recent result that these explosions will be visible at z = 10 - 20 to *JWST* and WFIRST. But they do demonstrate that multidimensional radiation transport will be required to model how radiation is emitted by and escapes from the complex structures formed by dynamical instabilities. This will be key to obtaining more realistic light curves and spectra for PPISNe. In future papers, we will better survey PPISN explosions by examining more progenitor models at low metallicities with 2D radiation hydrodynamical calculations (Zhang et al. 2013). PPISNe will soon open new windows on massive star

formation in both the primordial and the local universe.

The authors thank the anonymous referee for reviewing this manuscript and providing valuable comments, and the members of CCSE at LBNL for help with CASTRO. We also thank Volker Bromm, Dan Kasen, Lars Bildsten, John Bell, and Adam Burrows for many useful discussions. K.C. was supported by an IAU-Gruber Fellowship, a Stanwood Johnston Fellowship, and a KITP Graduate Fellowship. S.W. acknowledges support by DOE HEP Program under contract de-sc0010676; the National Science Foundation (AST 0909129) and the NASA Theory Program (NNX14AH34G). A.H. was supported by a Future Fellowship from the Australian Research Council (ARC FT 120100363). DJW was supported by the Baden-Württemberg-Stiftung by contract research via the programme Internationale Spitzenforschung II (grant P-LS-SPII/18). All numerical simulations were performed at the University of Minnesota Supercomputing Institute and the National Energy Research Scientific Computing Center. This work has been supported by the DOE grants de-sc0010676, DE-AC02-05CH11231, DE-GF02-87ER40328, DE-FC02-09ER41618 and by NSF grants AST-1109394 and PHY02-16783. Work at LANL was done under the auspices of the National Nuclear Security Administration of the US Department of Energy at Los Alamos National Laboratory under Contract No. DE-AC52-06NA25396.

REFERENCES

Almgren, A. S., et al. 2010, ApJ, 715, 1221

Barkat, Z., Rakavy, G., & Sack, N. 1967, Physical Review Letters, 18, 379

Blinnikov, S. I., Röpke, F. K., Sorokina, E. I., Gieseler, M., Reinecke, M., Travaglio, C., Hillebrandt, W., & Stritzinger, M. 2006, A&A, 453, 229

Bromm, V., & Yoshida, N. 2011, ARA&A, 49, 373

Bromm, V., Yoshida, N., Hernquist, L., & McKee, C. F. 2009, Nature, 459, 49

Chandrasekhar, S. 1961, Hydrodynamic and hydromagnetic stability, ed. Chandrasekhar, S.

Chatzopoulos, E., & Wheeler, J. C. 2012a, ApJ, 748, 42

—. 2012b, ApJ, 760, 154

Chatzopoulos, E., Wheeler, J. C., & Couch, S. M. 2013, ApJ, 776, 129

Chen, K., Heger, A., & Almgren, A. S. 2011, Computer Physics Communications, 182, 254

Chen, K.-J., Heger, A., & Almgren, A. S. 2013, Astronomy and Computing, 34, 70

Chen, K.-J., Heger, A., Woosley, S., Almgren, A., & Whalen, D. 2014, ArXiv e-prints

Chevalier, R. A., & Imamura, J. N. 1982, ApJ, 261, 543

Chevalier, R. A., & Irwin, C. M. 2011, ApJ, 729, L6

—. 2012, ApJ, 747, L17

Colella, P., & Woodward, P. R. 1984, Journal of Computational Physics, 54, 174

Cooke, J., et al. 2012, Nature, 491, 228

Dessart, L., Hillier, D. J., Waldman, R., Livne, E., & Blondin, S. 2012, MNRAS, 426, L76

Dessart, L., Waldman, R., Livne, E., Hillier, D. J., & Blondin, S. 2013, MNRAS, 428, 3227

Gal-Yam, A., et al. 2009, Nature, 462, 624

Glover, S. 2013, in Astrophysics and Space Science Library, Vol. 396, Astrophysics and Space Science Library, ed. T. Wiklind, B. Mobasher, & V. Bromm, 103

Heger, A., & Woosley, S. E. 2002, ApJ, 567, 532

Heger, A., Woosley, S. E., Martínez-Pinedo, G., & Langanke, K. 2001, ApJ, 560, 307

Herant, M., & Woosley, S. E. 1994, ApJ, 425, 814

Hummel, J. A., Pawlik, A. H., Milosavljević, M., & Bromm, V. 2012, ApJ, 755, 72

Imamura, J. N., Wolff, M. T., & Durisen, R. H. 1984, ApJ, 276, 667

Ivezic, Z., et al. 2008, arXiv:0805.2366

Joggerst, C. C., Almgren, A., Bell, J., Heger, A., Whalen, D., & Woosley, S. E. 2010, ApJ, 709, 11

Johnson, J. L., Whalen, D. J., Even, W., Fryer, C. L., Heger, A., Smidt, J., & Chen, K.-J. 2013, arXiv:1304.4601

Kaiser, N., et al. 2002, in Society of Photo-Optical Instrumentation Engineers (SPIE) Conference Series, Vol. 4836, Society of Photo-Optical Instrumentation Engineers (SPIE) Conference Series, ed. J. A. Tyson & S. Wolff, 154–164

Kasen, D., & Bildsten, L. 2010, ApJ, 717, 245

Kasen, D., Woosley, S. E., & Heger, A. 2011, ApJ, 734, 102

Law, N. M., et al. 2009, PASP, 121, 1395

Leloudas, G., et al. 2012, A&A, 541, A129

Mackey, J., Bromm, V., & Hernquist, L. 2003, ApJ, 586, 1

Moriya, T. J., Blinnikov, S. I., Tominaga, N., Yoshida, N., Tanaka, M., Maeda, K., & Nomoto, K. 2013, MNRAS, 428, 1020

Pan, T., Kasen, D., & Loeb, A. 2012, MNRAS, 422, 2701

Ritter, J. S., Safranek-Shrader, C., Gnat, O., Milosavljević, M., & Bromm, V. 2012, ApJ, 761, 56

Safranek-Shrader, C., Milosavljevic, M., & Bromm, V. 2013, arXiv:1307.1982

Scannapieco, E., Madau, P., Woosley, S., Heger, A., & Ferrara, A. 2005, ApJ, 633, 1031

Sedov, L. I. 1959, Similarity and Dimensional Methods in Mechanics, ed. Sedov, L. I.

Smith, B. D., & Sigurdsson, S. 2007, ApJ, 661, L5

Smith, B. D., Turk, M. J., Sigurdsson, S., O'Shea, B. W., & Norman, M. L. 2009, ApJ, 691, 441

Timmes, F. X., & Swesty, F. D. 2000, ApJS, 126, 501

Vink, J. S. 2014, ArXiv e-prints

Volonteri, M. 2012, Science, 337, 544

Weaver, T. A., Zimmerman, G. B., & Woosley, S. E. 1978, ApJ, 225, 1021

Whalen, D., Abel, T., & Norman, M. L. 2004, ApJ, 610, 14

Whalen, D. J. 2012, arXiv:1209.4688

Whalen, D. J., Fryer, C. L., Holz, D. E., Heger, A., Woosley, S. E., Stiavelli, M., Even, W., & Frey, L. H. 2013a, ApJ, 762, L6

Whalen, D. J., Joggerst, C. C., Fryer, C. L., Stiavelli, M., Heger, A., & Holz, D. E. 2013b, ApJ, 768, 95

Whalen, D. J., Smidt, J., Even, W., Woosley, S. E., Heger, A., Stiavelli, M., & Fryer, C. L. 2014, ApJ, 781, 106

Whalen, D. J., et al. 2013c, ApJ, 777, 110

—. 2013d, ApJ, 768, 195

—. 2013e, ApJ, 778, 17

Woosley, S. E. 2010, ApJ, 719, L204

Woosley, S. E., Blinnikov, S., & Heger, A. 2007, Nature, 450, 390

Zhang, W., Howell, L., Almgren, A., Burrows, A., & Bell, J. 2011, ApJS, 196, 20

Zhang, W., Howell, L., Almgren, A., Burrows, A., Dolence, J., & Bell, J. 2013, ApJS, 204, 7

This manuscript was prepared with the AAS LaTeX macros v5.2.

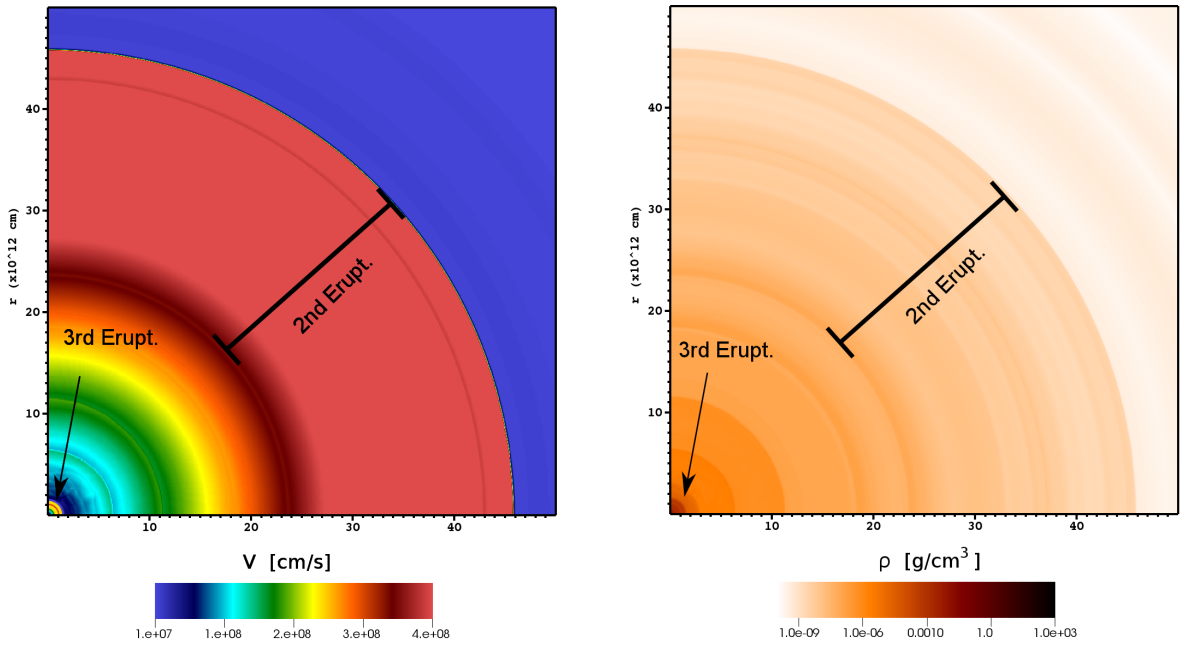

Fig. 1.— Velocities and densities at the time P3 is ejected. Minor perturbations in fluid velocities due to fallback from P2 are visible near the surface of the core of the star. The overall density distribution is still spherically symmetric.

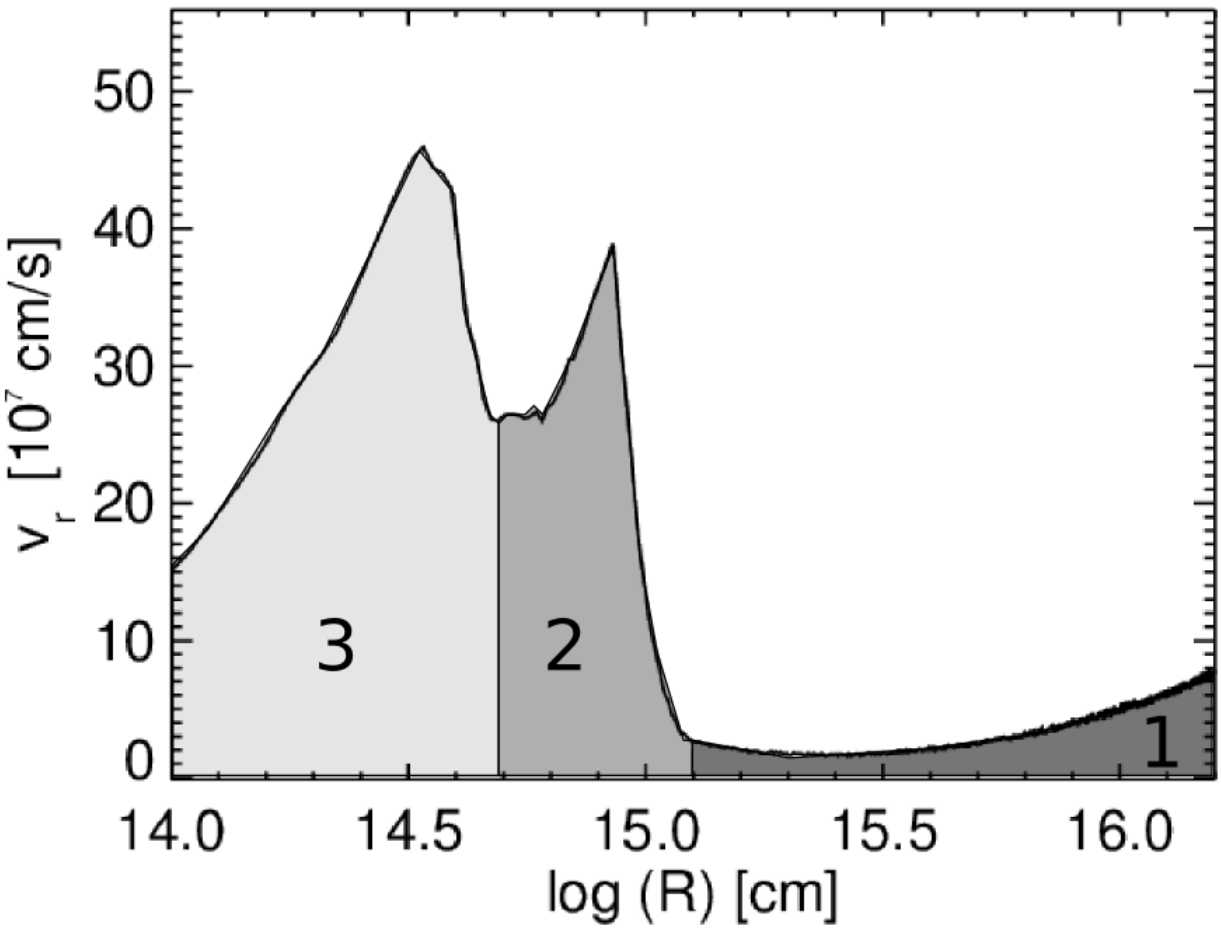

Fig. 2.— Radial velocities at the beginning of the CASTRO run. The shaded areas mark the ejecta from different eruptions. P3 has the highest peak velocity, catching up first to P2 and then eventually to P1.

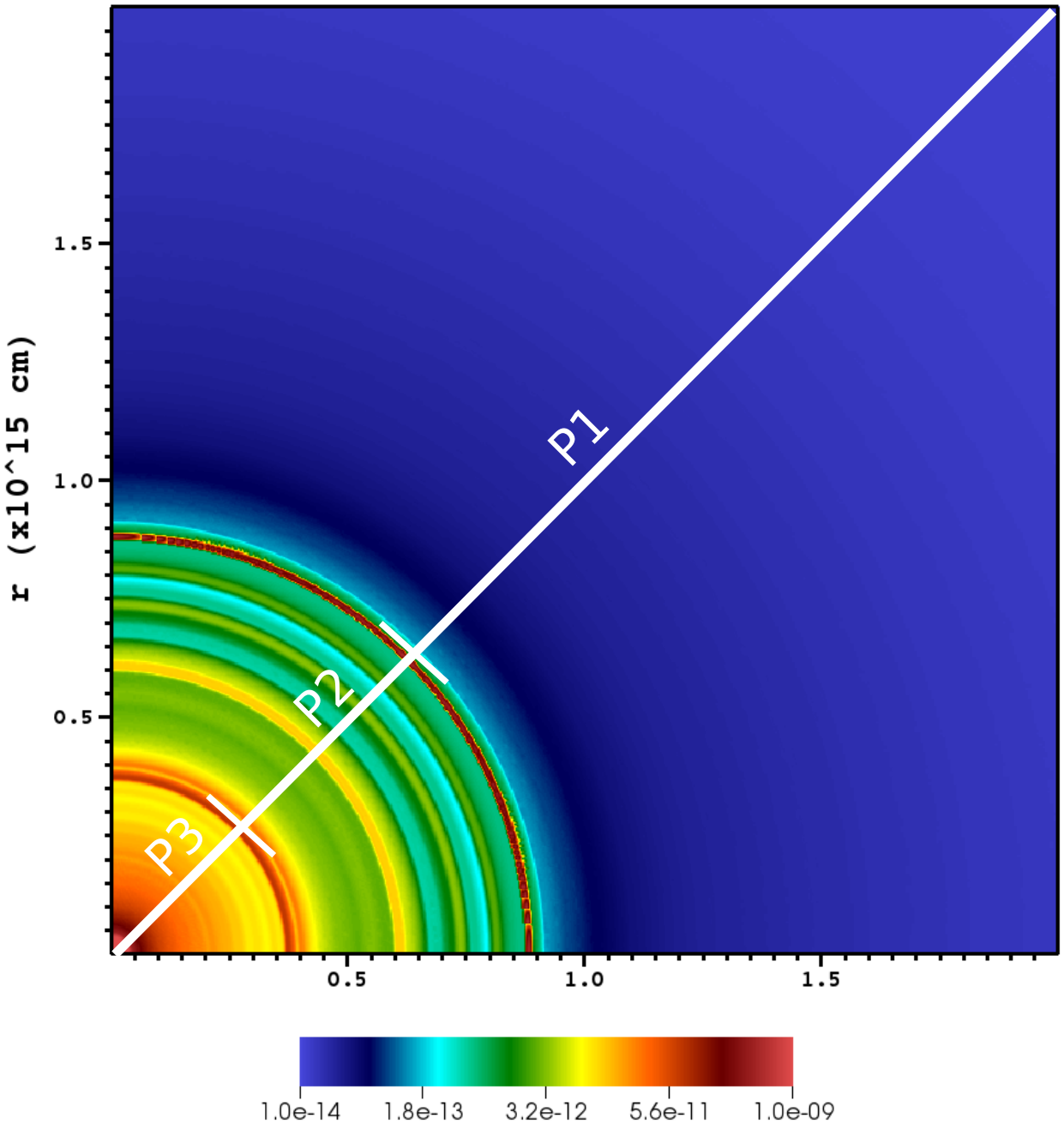

Fig. 3.— Densities at the beginning of the CASTRO run. The white tick marks mark the boundaries of P1, P2, and P3. The finest structure is mostly associated with P2. Note that at the time of launch the mass distribution of the star is spherically symmetric.

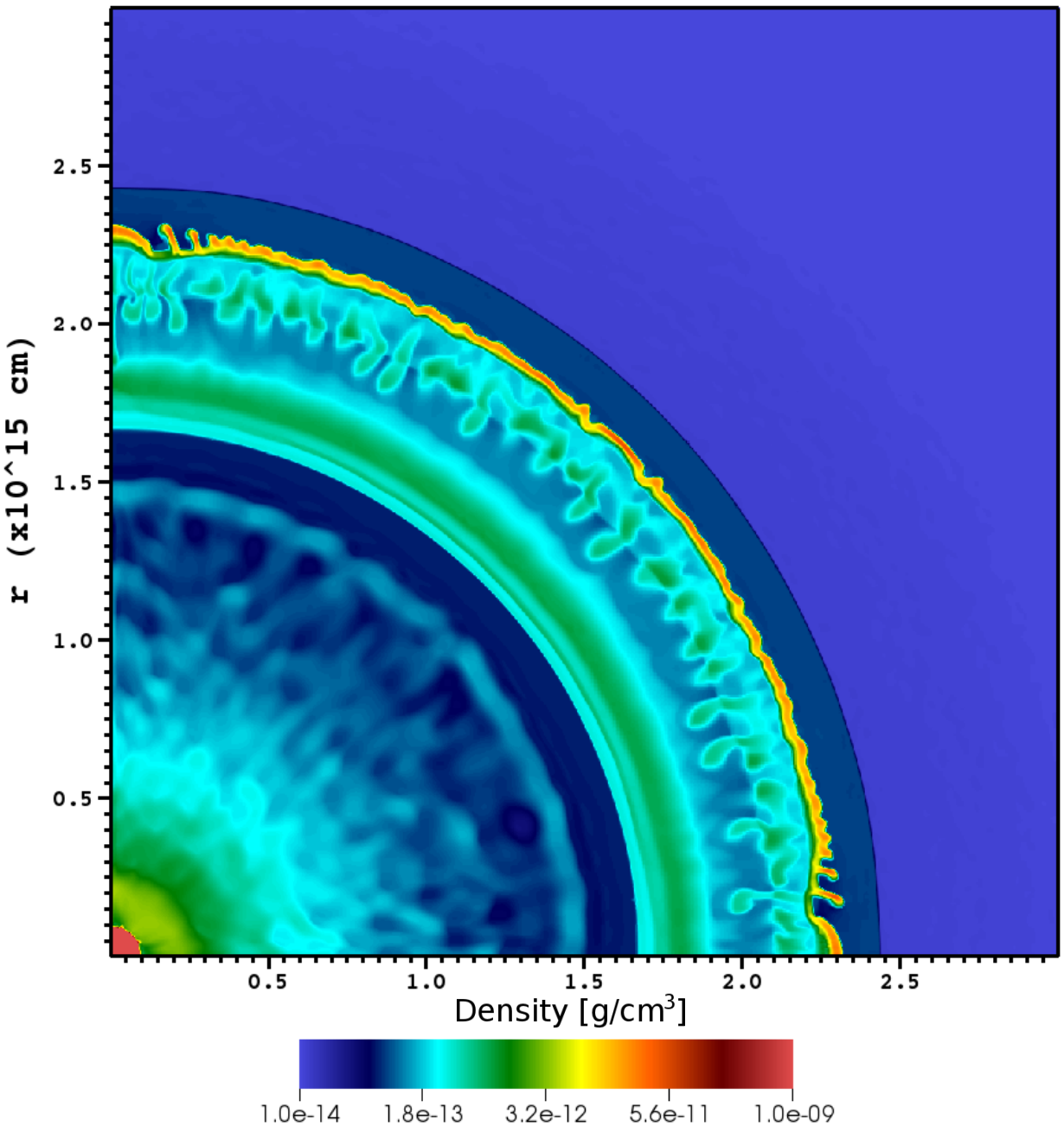

Fig. 4.— Densities after P3 collides with P2. Mild fluid instabilities have formed and created the density fingers at the site of the collision.

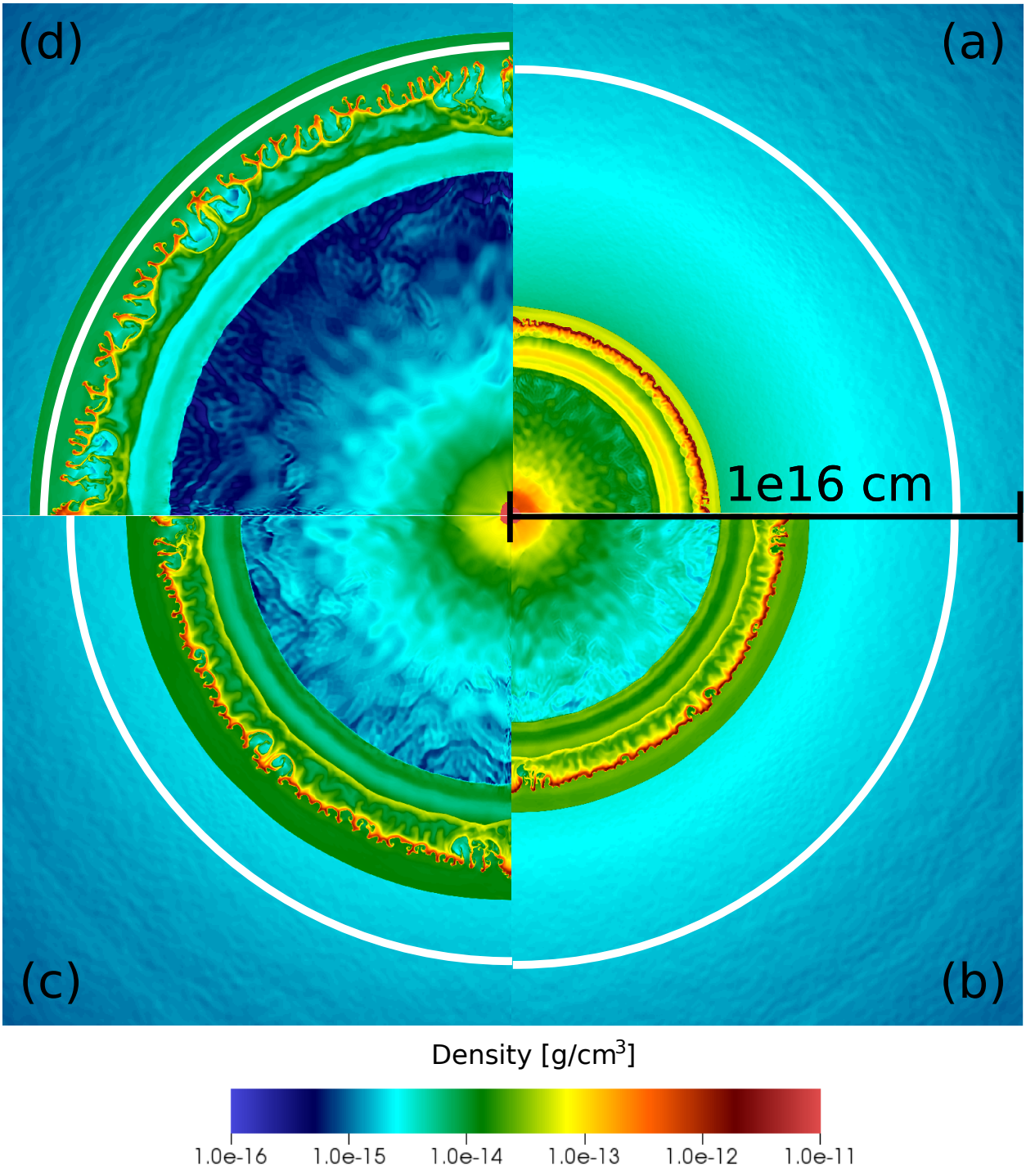

Fig. 5.— The growth of fluid instabilities and expansion of the photosphere during the second collision. Panels (a) - (d) show the instabilities at 97, 149, 205, and 266 days, respectively (P2 and P3 have just merged in the first panel). The white arc in each panel is the photosphere. When the shell formed from P2 and P3 reaches 8×10^{15} cm, it becomes visible to an external observer (although most of the radiation from their collision has already been emitted).

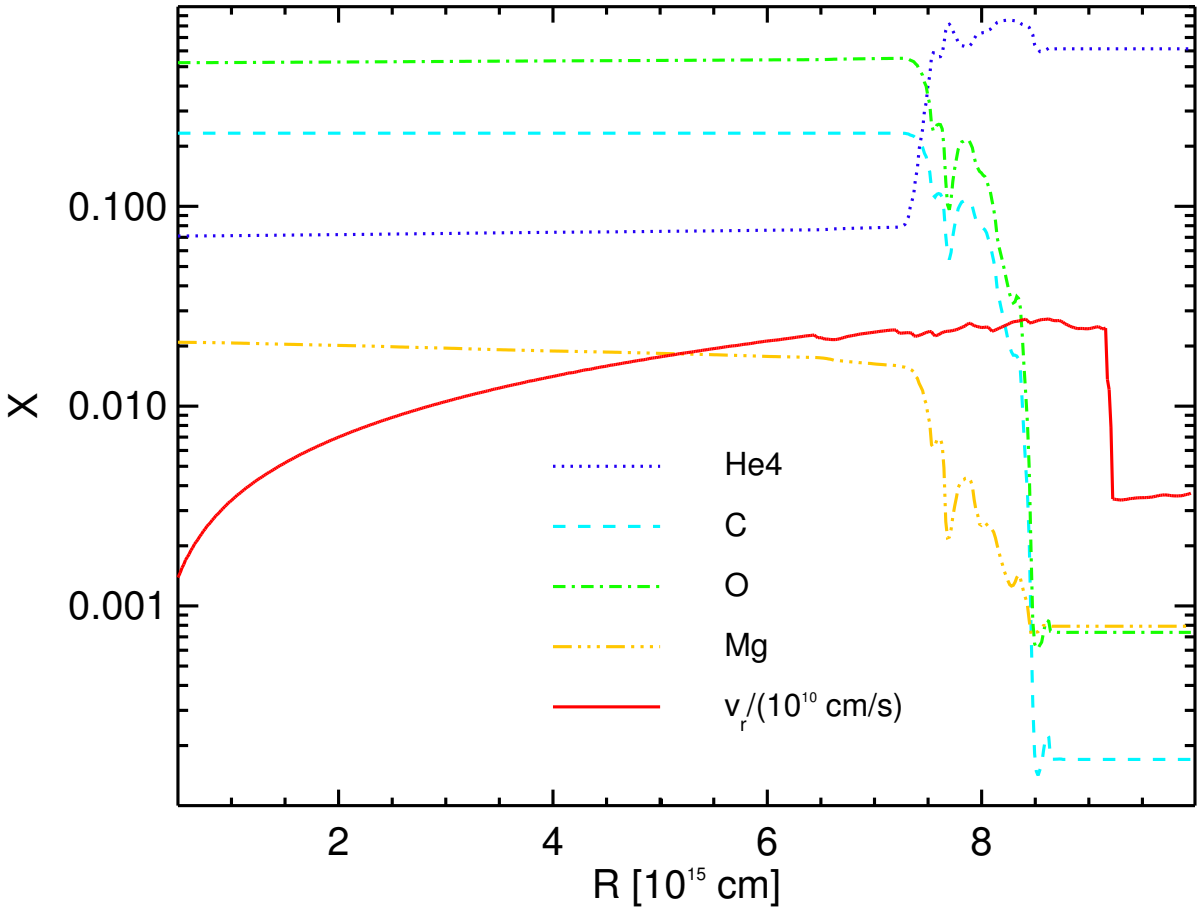

Fig. 6.— Mass fractions and velocities at 256 days. The elements that are dredged up are mostly ^{12}C and ^{16}O. Few elements heavier than ^{28}Si are ejected by the star, so they may not appear in PPISNe.

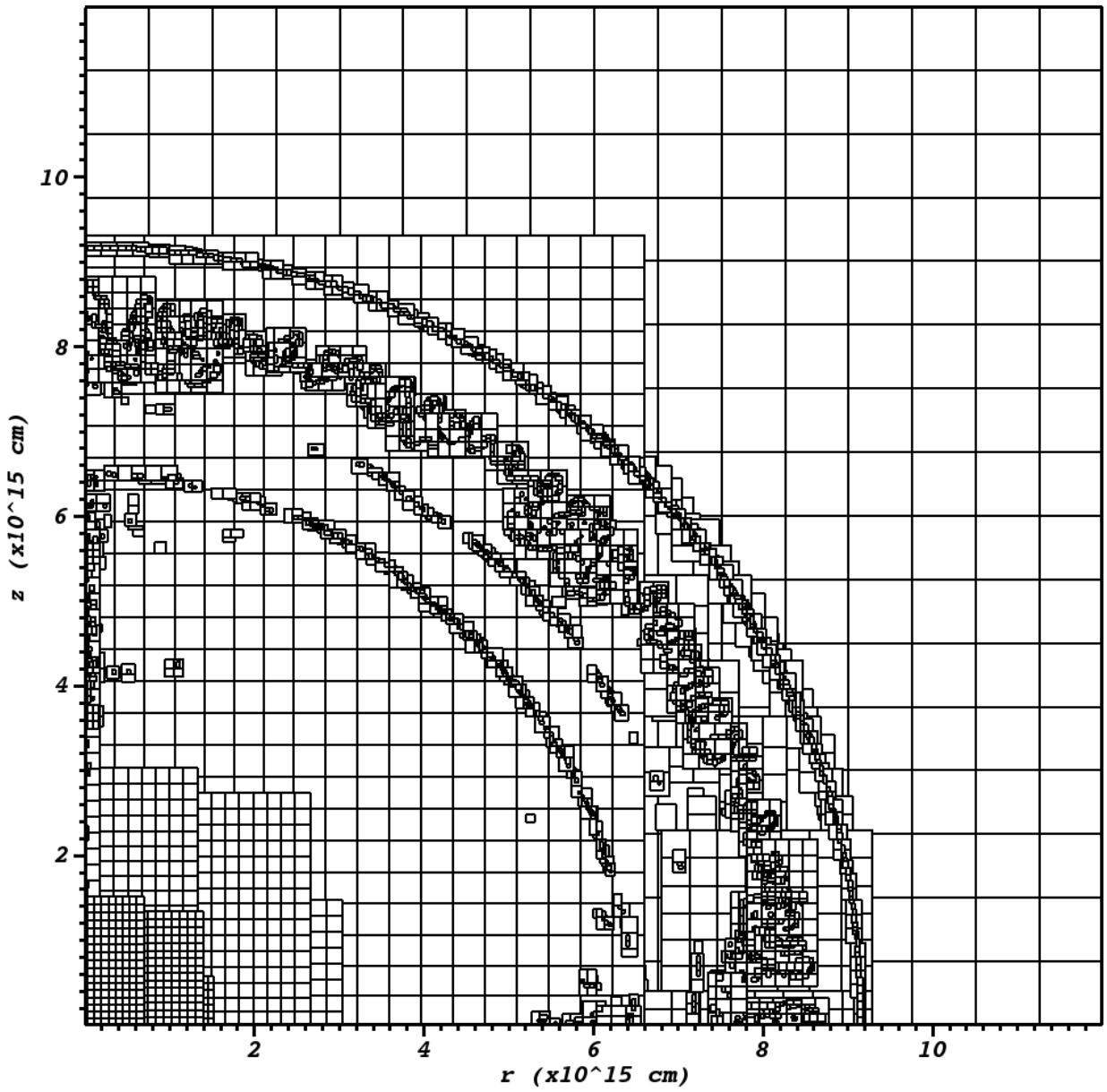

Fig. 7.— AMR grid structure during the shell collision. Smaller grids indicate more refined zones. Most of the fine grids are generated to resolve the colliding shells and the core of the star.

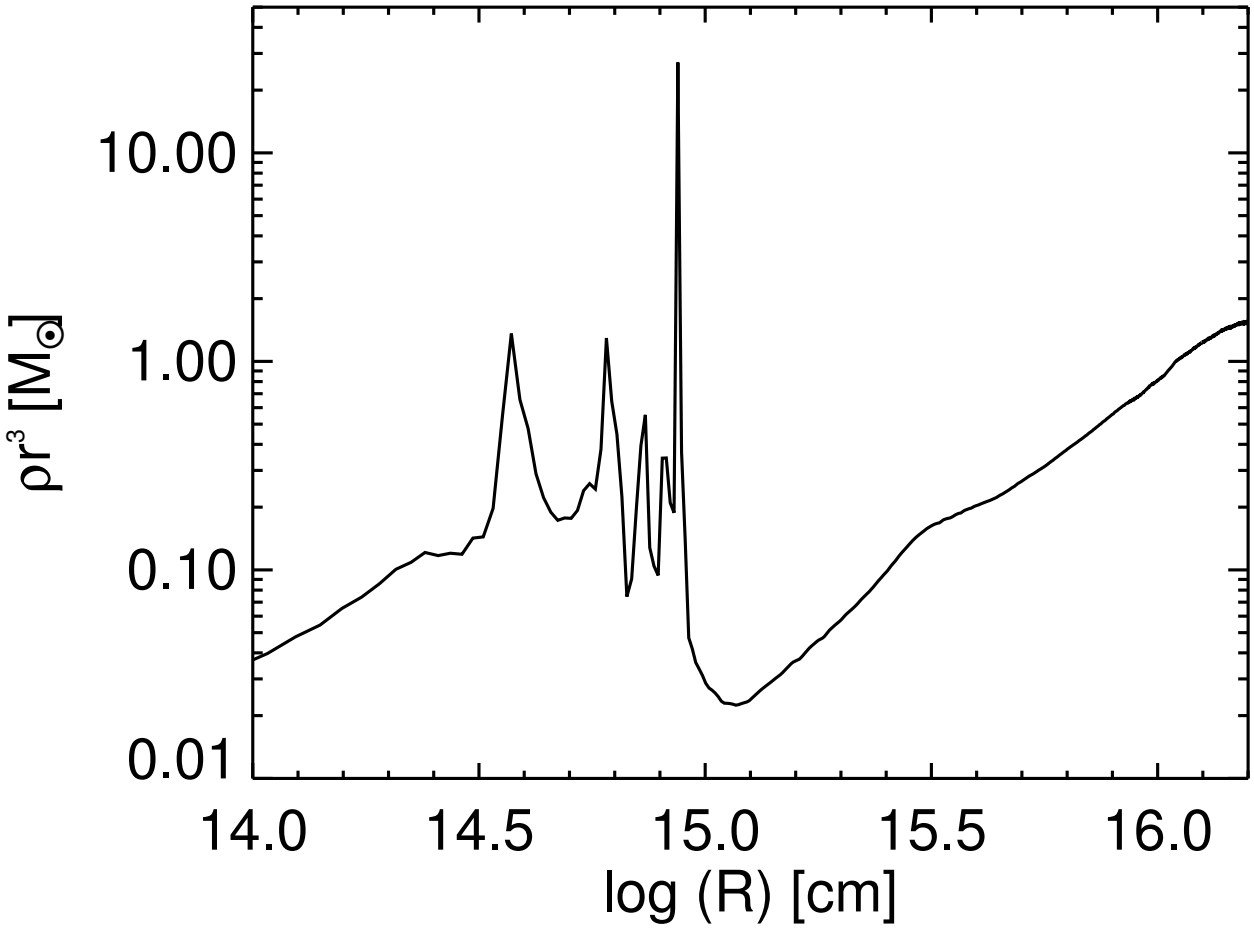

Fig. 8.— The $\rho\, r^3$ profile at the beginning of the CASTRO run. The ejection of P2 and P3 create the spiky pattern at $r < 10^{15}\,\mathrm{cm}$. The ejection and subsequent expansion of P1 creates an extended and more homogeneous envelope, which is visible as the steady rise of $\rho\, r^3$ at $r \geq 10^{15}\,\mathrm{cm}$.

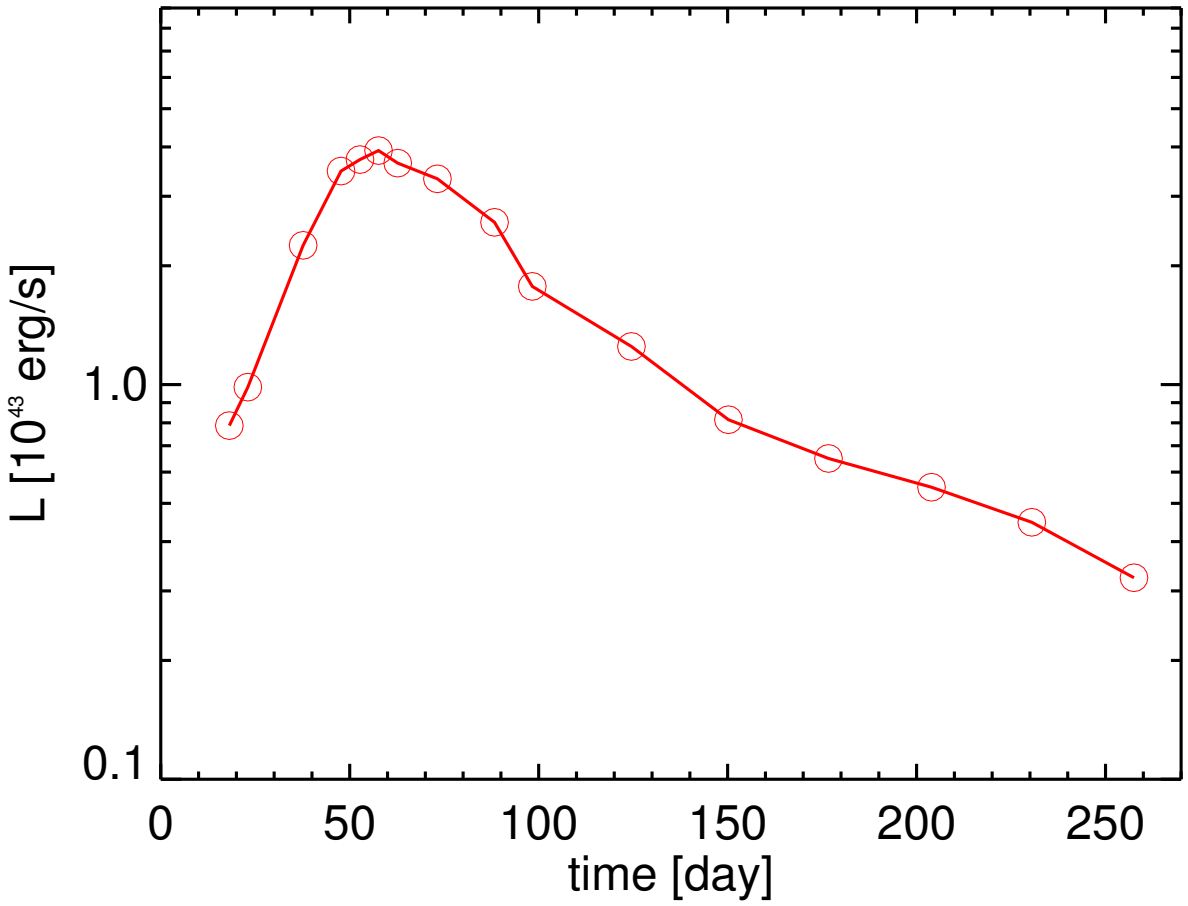

Fig. 9.— Light curve of shell collision. The red circles represent the snapshots from the simulation. It luminosity peaks at 4×10^{43} erg sec^{-1} and the duration of emission lasts for 100 days.